ACS NANO

www.acsnano.org

ARTICLE

In-Situ Crafting of $ZnFe_2O_4$ Nanoparticles Impregnated within Continuous Carbon Network as Advanced Anode Materials

Beibei Jiang, Cuiping Han, Bo Li, Yanjie He, and Zhiqun Lin*

School of Materials Science and Engineering, Georgia Institute of Technology, Atlanta, Georgia 30332, United States

Supporting Information

ABSTRACT: The ability to create a synergistic effect of nanostructure engineering and its hybridization with conductive carbonaceous material is highly desirable for attaining high-performance lithium ion batteries (LIBs). Herein, we judiciously crafted $ZnFe_2O_4$/carbon nanocomposites composed of $ZnFe_2O_4$ nanoparticles with an average size of 16 ± 5 nm encapsulated within the continuous carbon network as anode materials for LIBs. Such intriguing nanocomposites were yielded *in situ via* the pyrolysis-induced carbonization of polystyrene@poly(acrylic acid) (PS@PAA) core@shell nanospheres in conjunction with the formation of $ZnFe_2O_4$ nanoparticles through the thermal decomposition of $ZnFe_2O_4$ precursors incorporated within the PS@PAA nanospheres. By systematically varying the $ZnFe_2O_4$ content in the $ZnFe_2O_4$/carbon nanocomposites, the nanocomposite containing 79.3 wt % $ZnFe_2O_4$ was found to exhibit an excellent rate performance with high capacities of 1238, 1198, 1136, 1052, 926, and 521 mAh g^{-1} at specific currents of 100, 200, 500, 1000, 2000, and 5000 mA g^{-1}, respectively. Moreover, cycling performance of the $ZnFe_2O_4$/carbon nanocomposite with 79.3 wt % $ZnFe_2O_4$ at specific currents of 200 mA g^{-1} delivered an outstanding prolonged cycling stability for several hundred cycles.

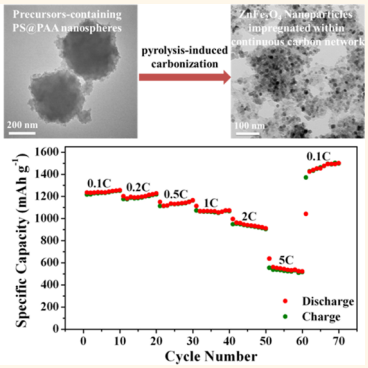

KEYWORDS: *$ZnFe_2O_4$ nanoparticles, continuous carbon network, advanced anode, lithium-ion batteries*

An enormous spectrum of applications of lithium-ion batteries (LIBs), particularly in electric vehicles (EVs), hybrid EVs, and electric grids, invokes essential requirements on their energy storage capabilities. In this context, considerable efforts have been devoted to the development of advanced electrodes with high energy density and power density as well as long cycle life at low cost.[1] However, the most common commercial graphite anode material still exhibits a relatively low theoretical specific capacity of 372 mAh g^{-1}, which cannot meet the demand of the high-energy applications noted above.[2] To date, a wide variety of anode materials with much higher capacities have been extensively investigated. In this regard, transition metal oxides (M_xO_y, where M is Fe, Co, Ni, Cu, Sn, Mn, *etc.*) clearly stand out as the promising alternatives to graphite owing to their attractive higher theoretical capacities (>600 mAh g^{-1}), low cost, environmental friendliness, and wide availability containing earth-abundant elements.[2−4] Lithium storage within transition metal oxides is mainly achieved through the reversible conversion reaction between lithium ions and metal oxides, which form metal nanocrystals dispersed in the Li_2O matrix, that is, $M_xO_y + 2yLi \leftrightarrow xM + yLi_2O$.[3,5] For example, Fe_3O_4 as a green and naturally abundant material reacts with eight lithium ions completely per formula unit, offering a theoretical capacity of 926 mAh g^{-1}. Moreover, the conductivity of Fe_3O_4 is as high as 10^2 S cm^{-1}, much larger than other metal oxide active materials such as TiO_2 (10^{-10} S cm^{-1}) and SnO_2 (10^{-3} S cm^{-1}),[6,7] making it an attractive anode material for achieving high energy density and power density. By replacing one iron atom with zinc, the resulting ternary oxide (*i.e.*, $ZnFe_2O_4$) contributes an extra lithium uptake by forming LiZn alloy, leading to an enhanced theoretical capacity of 1000.5 mAh g^{-1}.[5]

Despite the intriguing features described above, these high-capacity transition metal oxide anode materials have not yet been implemented for practical applications. This is due to their capacity decay over cycling which originates primarily from the electrode pulverization and the subsequent loss of electrical contacts between the active materials and the current collectors caused by the volume change-induced stress during the repeated insertion and extraction of lithium ions.[8,9] Another challenging issue concerns the poor electrical conductivity of transition metal oxides, which limits the attainable high capacity at high a charge/discharge rate.[3]

Two main strategies have been widely recognized as effective methods in alleviating these issues. The first strategy is to utilize

Received: December 11, 2015
Accepted: January 19, 2016
Published: January 19, 2016

DOI: 10.1021/acsnano.5b07806
ACS Nano 2016, 10, 2728−2735

nanostructured active materials which are advantageous because of (i) a better accommodation of mechanical stress,[10,11] (ii) the shortened transport length for electrons and lithium ions and thus rendering fast discharging/charging,[12,13] and (iii) a higher electrode/electrolyte contact area favorable for improving the lithium reaction rate.[14,15] Nanosized transition metal oxides in various morphologies such as nanoparticles,[3,16,17] nanotubes,[18] nanorods/nanowires,[19−21] nanospindles,[22] nanosheets,[23] *etc.* have been demonstrated to offer opportunities in achieving superior electrochemical performance. However, some problems may arise as a result of the high surface-to-volume ratio and the large surface energy of nanostructured active materials. These problems include undesirable electrode/electrolyte reactions,[14] repeated decomposition/formation of solid electrolyte interphase (SEI) films due to the cyclic exposure of active material surface to electrolyte *via* the generated transition metal nanocrystals, resulting in thick SEI films and a large irreversible capacity (*i.e.*, low columbic efficiency).[3]

The second strategy for improving the electrochemical performance involves the construction of hybrid nanomaterials with more conductive carbonaceous materials (*e.g.*, porous carbon, carbon nanotubes, nanofibers, graphene/graphite, *etc.*). Carbonaceous materials possess good electronic conductivity and high rate capability.[24,25] Moreover, they have the capability of preserving the structural integrity of active materials, thereby entailing enhanced cyclability and rate capacity in the resulting hybrid composites.[26] A diversity of modifications with carbonaceous materials have been exploited, such as surface carbon coating,[3,5,27−29] graphene as substrate with active nanomaterials decorating, growing or anchoring on the surface,[30−33] graphene/carbon encapsulated active materials,[3,9,34] mechanically mixing graphene with active materials,[35] graphene nanosheets wrapped active material particles,[36] sandwich-like graphene/active material/graphene structures,[37] layered structures with active materials alternating with graphene sheets,[38] *etc.* Clearly, the synergy of the two strategies noted above, that is, nanostructure engineering and its hybridization with conductive carbonaceous material, would impart a better electrochemical performance. However, it remains challenging to achieve this synergy.

Herein, we report a robust *in situ* crafting of $ZnFe_2O_4$/carbon nanocomposites electrode composed of $ZnFe_2O_4$ nanoparticles with an average diameter of 16 ± 5 nm impregnated within the continuous carbon network via the pyrolysis of $ZnFe_2O_4$ precursors-containing polystyrene@poly(acrylic acid) (PS@PAA) core@shell nanospheres. The PS@PAA nanospheres were synthesized in *one-step* by emulsion polymerization, followed by thermal annealing of $ZnFe_2O_4$ precursor-containing PS@PAA nanospheres, leading to the formation of $ZnFe_2O_4$ nanoparticles embedded in the continuous carbon network due to the carbonization of PS@PAA nanospheres. Intriguingly, the PS@PAA nanospheres not only functioned as templates by incorporating $ZnFe_2O_4$ precursors (*i.e.*, $Zn(NO_3)_2{\cdot}6H_2O$ and $Fe(NO_3)_3{\cdot}9H_2O$) in the region occupied by the PAA shell owing to a strong coordination bonding between the carboxyl groups of PAA and the metal moieties of precursors,[39,40] but also acted as the polymeric source for the creation of carbon network. By carefully performing thermal annealing under argon atmosphere, the precursor-containing PS@PAA nanospheres decomposed slowly, accompanied by the collapse, shrinkage, and carbonization of polymers with the formation of $ZnFe_2O_4$ nanoparticles. The mass content of $ZnFe_2O_4$ nanoparticles in $ZnFe_2O_4$/C nanocomposites was systematically varied. The optimal content of 79.3 wt % $ZnFe_2O_4$ was found to yield the best rate capability for LIBs. It is noteworthy that the carbon network provides a continuous and conductive pathway for electron transport, resulting in excellent rate capability when $ZnFe_2O_4$/carbon nanocomposites containing 79.3 wt % $ZnFe_2O_4$ were evaluated as potential anode materials with high capacities of 1238, 1198, 1136, 1052, 926, and 521 mAh g^{-1} at specific currents of 100, 200, 500, 1000, 2000, and 5000 mA g^{-1}, respectively. In addition, the carbon network renders the mechanical flexibility of active materials, as well as retains the structural integrity of $ZnFe_2O_4$/carbon nanocomposites during repeated lithiation/delithiation, thereby leading to a prolonged cyclic life of the $ZnFe_2O_4$/carbon electrode (>98% capacity retention after cycling at 200 mA g^{-1} for over 400 cycles).

RESULTS AND DISCUSSION

Emulsion polymerization is a very inexpensive and environmental friendly chemical process. A typical emulsion polymerization comprises a hydrophobic monomer, water, an oil-in-water surfactant, and a water-soluble initiator. At the beginning of emulsion polymerization, the monomer droplets having large oil−water interfacial area are emulsified through physically absorbing or chemically incorporating the surfactant. The surfactant serves primarily for controlling the latex particle size and stabilizing the particles at high concentration. With the addition of initiators, the polymerization proceeds.[41] In the present study of forming PS@PAA core@shell nanospheres, hydrophobic monomers of styrene and hydrophilic monomers of acrylic acid were first dispersed in water, forming uniform oil-in-water droplets. The polymerization of oil-in-water droplets of styrene and the creation of free radical of acrylic acid were initiated by the initiator $K_2S_2O_8$. The resulting PS formed the core of the core@shell nanospheres (upper left panel in Figure 1). Interestingly, on the other hand, a small portion of hydrophilic acrylic acid monomers and their

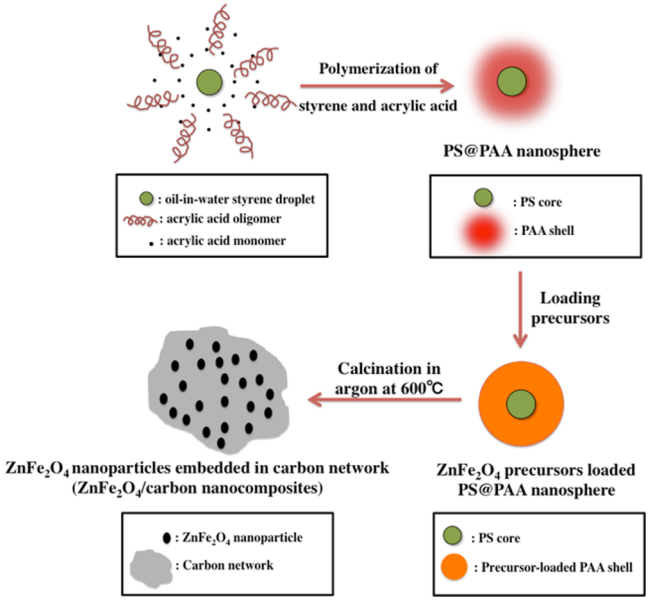

Figure 1. Schematic illustration of the formation of PS@PAA nanospheres and the resulting $ZnFe_2O_4$/carbon nanocomposites comprising $ZnFe_2O_4$ nanoparticles impregnated within the carbon network.

DOI: 10.1021/acsnano.5b07806
ACS Nano 2016, 10, 2728−2735

resulting oligomers acted as surfactant to stabilize the oil-in-water droplets noted above (upper left panel in Figure 1).[42] In the meantime, a great portion of hydrophilic acrylic acid monomers was dissolved in water and further polymerized to yield oligomers. As the polymerization continues, the molecular weight of the formed acrylic acid oligomers increased, leading to the decrease in hydrophilicity of acrylic acid oligomers and the formation of PAA. The coagulation of PAA on the PS core produced the PAA shell, and thus PS@PAA core@shell nanospheres (upper right panel in Figure 1).[42]

The transmission electron microscopy (TEM) image for the PS@PAA nanospheres clearly showed their core@shell structure with an average diameter of approximately 260 nm (Figure 2a). After the polymerization was complete by reacting at 80 °C for 24 h, the precursors solution (*i.e.*, $Zn(NO_3)_2{\cdot}6H_2O$ and $Fe(NO_3)_3{\cdot}9H_2O$ dissolved in water) with controlled amount and pH value was added dropwise to the PS@PAA nanospheres solution at 80 °C under vigorous stirring. As the carboxyl group of PAA has a strong coordination interaction with Fe^{3+} and Zn^{2+} ions,[39,40,43] the PS@PAA nanospheres functioned as templates by incorporating $ZnFe_2O_4$ precursors, yielding the $ZnFe_2O_4$ precursors-loaded PS@PAA nanospheres (Figure 2b). In comparison with pure PS@PAA nanospheres, the edges of the PAA shell was blurred by the precursors, suggesting the success in loading $ZnFe_2O_4$ precursors.

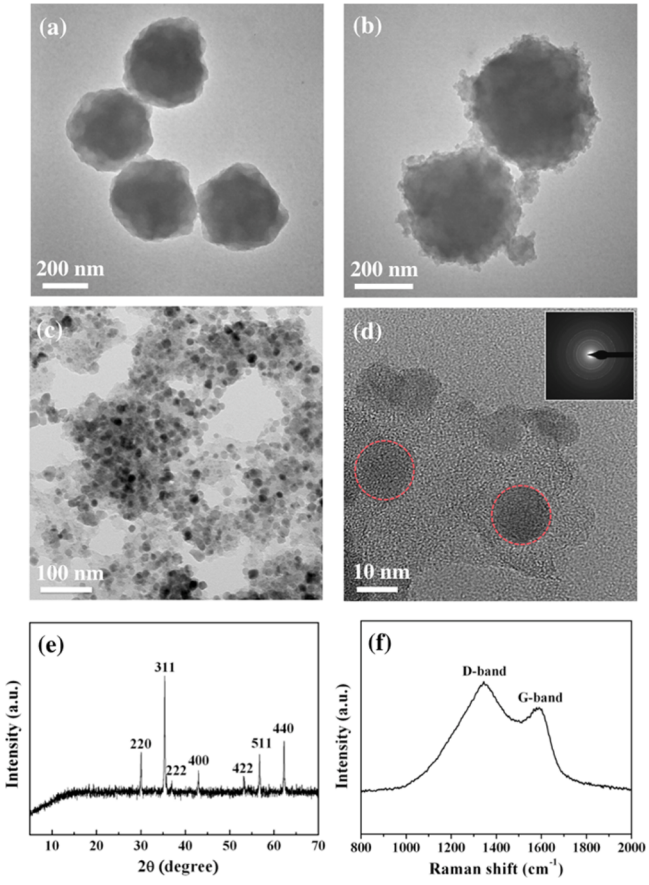

Figure 2. Sample characterizations. TEM images of (a) PS@PAA core@shell nanospheres, (b) $ZnFe_2O_4$ precursors-loaded PS@PAA nanospheres, and (c) the $ZnFe_2O_4$(79.3 wt %)/carbon nanocomposites formed after calcination in argon at 600 °C with $ZnFe_2O_4$ nanoparticles embedded within the continuous carbon network (the average diameter of $ZnFe_2O_4$ nanoparticles is 16 ± 5 nm). The corresponding HRTEM image of panel c is shown in panel d, where the $ZnFe_2O_4$ nanoparticles are marked in red circles. The inset in panel d is the SAED pattern of $ZnFe_2O_4$/carbon nanocomposites. (e) XRD pattern of $ZnFe_2O_4$(79.3 wt %)/carbon nanocomposites. (f) Raman spectra of $ZnFe_2O_4$(79.3 wt %)/carbon nanocomposites. The excitation wavelength is 785 nm.

Fourier transform infrared spectroscopy (FTIR) spectra of PS@PAA nanospheres before and after the introduction of $ZnFe_2O_4$ precursors were also measured to further confirm the loading of precursors. As shown in Figure S1, the characteristic absorption at 3023, 2921, 1600, 1493, 1452, 1025, 757, and 697 cm^{-1} corresponding to benzene rings[44] in the PS core and the characteristic peak at 1709 cm^{-1} attributed to the carboxylic acid group of PAA[45] are clearly evident in as-prepared PS@PAA nanospheres. After the loading of $ZnFe_2O_4$ precursors, a strong peak at 1385 cm^{-1} corresponding to the NO_3^- ions[46] emerged, signifying that the precursors (*i.e.*, $Zn(NO_3)_2{\cdot}6H_2O$ and $Fe(NO_3)_3{\cdot}9H_2O$) were successfully incorporated within the space occupied by the PAA shell of PS@PAA core/shell nanospheres. Notably, the peaks corresponding to PS core and PAA shell became weaker after the loading of precursors.

The $ZnFe_2O_4$ precursors-containing PS@PAA nanospheres provided a good source for the formation of $ZnFe_2O_4$ nanoparticles (from precursors) and the creation of a carbon network (from PS@PAA nanospheres). The thermogravimetric analysis (TGA) of the $ZnFe_2O_4$ precursors-loaded PS@PAA nanospheres in nitrogen atmosphere showed a significant weight loss at around 400 °C due to the degradation of PS and PAA; the weight loss was then slowed over a temperature range of 400−600 °C (Figure S2). After 600 °C, the weight remained nearly constant, implying that the thermal decomposition process was complete. Thus, 600 °C was chosen as the temperature for the calcination treatment as higher temperature may result in the reduction of $ZnFe_2O_4$ by the formed carbon.[47]

The calcination of the precursors-loaded PS@PAA nanospheres under argon atmosphere at a ramping rate of 1 °C/min for 2 h led to the thermal decomposition of both the PS@PAA nanospheres and the loaded precursors, converting the precursors into $ZnFe_2O_4$ nanoparticles in conjunction with the collapse and shrinkage of PS@PAA nanospheres and their final transformation into carbon. It is noteworthy that the loading of precursors within the PAA core of PS@PAA nanospheres restricted the aggregation and coarsening of $ZnFe_2O_4$ nanoparticles during the high-temperature treatment, thereby rendering the formation of $ZnFe_2O_4$ nanoparticles with an average diameter of 16 ± 5 nm dispersed in the continuous carbon network (*i.e.*, $ZnFe_2O_4$/carbon nanocomposites; Figure 2c,d). Figure 2d clearly shows the presence of continuous carbon network encapsulating $ZnFe_2O_4$ nanoparticles. The selected area electron diffraction (SAED) pattern (inset in Figure 2d) exhibited a series of concentric rings, signifying the polycrystalline characteristics of the resulting $ZnFe_2O_4$ nanoparticles.

The chemical composition of $ZnFe_2O_4$/carbon nanocomposites was analyzed by energy-dispersive X-ray spectroscopy (EDX). As shown in Figure S3, the elements of both Zn and Fe were observed, indicating the existence of $ZnFe_2O_4$. The formation of the $ZnFe_2O_4$ phase was further corroborated by the X-ray diffraction (XRD) measurement (Figure 2e). The XRD peaks at 30°, 35.5°, 38.0°, 43.5°, 53.2°, 56.7°, and 62.3° can be assigned to the [220], [311], [222], [400], [422], [511] and [440] planes of $ZnFe_2O_4$ in cubic spinel structure with *Fd*-3*m* space group (JCPDS Card No. 022-1012), which matched

DOI: 10.1021/acsnano.5b07806
ACS Nano 2016, 10, 2728−2735

very well with the previously reported results.[5,48] The absence of peaks assignable to the crystalline phase of carbon suggested the carbon network was likely in an amorphous state.

Raman spectroscopy measurement on $ZnFe_2O_4$/carbon nanocomposites was performed with an excitation wavelength of 785 nm. The peaks at around 1340 and 1590 cm^{-1} correspond to D band (disordered graphitic structure) and G band (graphitic structure) of carbon, respectively (Figure 2f). The large intensity ratio of I_D/I_G for the $ZnFe_2O_4$/carbon nanocomposites verified the amorphous nature of carbon,[49] correlating well with the XRD result.

It is well-known that the amount of carbon is a crucial parameter in determining the electrochemical performance of the nanocomposites electrode.[50,51] To optimize the electrochemical performance, we scrutinized $ZnFe_2O_4$/carbon nanocomposites at different $ZnFe_2O_4$ to carbon ratios by varying the molar ratio of $ZnFe_2O_4$ precursors to PS@PAA nanospheres. On the basis of the TGA results shown in Figure S4, the $ZnFe_2O_4$ contents in these $ZnFe_2O_4$/carbon nanocomposites were determined to be 61.4, 67.4, 74.5, 79.3, and 83.5 wt %, respectively. We note that the TEM, XRD, and Raman results described above are all from the $ZnFe_2O_4$/carbon nanocomposites containing 79.3 wt % $ZnFe_2O_4$ (hereafter referred to as $ZnFe_2O_4$(79.3 wt %)/carbon); and the other four nanocomposites samples showed similar results from these characterizations. It is notable that the precursors-loaded PS@PAA nanospheres were also calcinated in air, and the pure $ZnFe_2O_4$ nanoparticles without the carbon network encapsulation was obtained and used as control.

To scrutinize the lithiation and delithiation behavior of $ZnFe_2O_4$/carbon nanocomposites electrode, the cyclic voltammetry (CV) measurement on the $ZnFe_2O_4$(79.3 wt %)/carbon electrode was performed at a scan rate of 0.1 mV s^{-1} over a potential range from 0.005 to 3 V. Figure 3a shows the CVs for the first seven cycles. In the first cathodic scan, a broad peak at around 0.8 V was observed, which can be attributed to the reduction of Fe^{3+} and Zn^{2+} to their metallic states, the formation of Li−Zn alloys, and an irreversible reaction related to the decomposition of electrolyte.[52] The cathodic peak shifts to around 0.95 V in the subsequent scans, differentiating the later reduction mechanism from the one in the first scan. For the anodic scans, a broad peak centered at around 1.75 V was seen due to the oxidation of metallic Fe and Zn to Fe^{3+} and Zn^{2+}, respectively.[53] Moreover, the cathodic and anodic peaks did not shift in the subsequent cycles, confirming a highly reversible reaction with lithium once the initial structural changes were completed.

Figure 3b presents the galvanostatic discharge/charge profiles of $ZnFe_2O_4$(79.3 wt %)/carbon nanocomposites electrode over a voltage range from 0.005 to 3 V at specific current of 100 mA g^{-1} for the first 10 cycles. The initial discharge profile showed a voltage plateau at around 0.8 V. It was then shifted to approximately 0.95 V for the subsequent cycles, consistent with the CV results discussed above. The charge profiles displayed a voltage plateau at about 1.75 V for the first 10 cycles, indicating high reversibility. The initial discharge and charge capacities for $ZnFe_2O_4$(79.3 wt %)/carbon nanocomposites anode are 1626 mAh g^{-1} and 1206 mAh g^{-1}, respectively, with the initial Coulombic efficiency of 74.2% (all specific capacities are calculated based on the net weight of $ZnFe_2O_4$ nanoparticles). The initial irreversible capacity loss was probably due to the initial lithiation of $ZnFe_2O_4$ which irreversibly consumed extra lithium and the formation of solid electrolyte interface (SEI) layer at the electrode/electrolyte interface caused by the reduction of electrolyte.[31] For the subsequent cycles, the discharge and charge capacities were stabilized at around 1200 mAh g^{-1} with Coulombic efficiencies approaching 100%, signifying a high reversibility of lithium uptake and release.

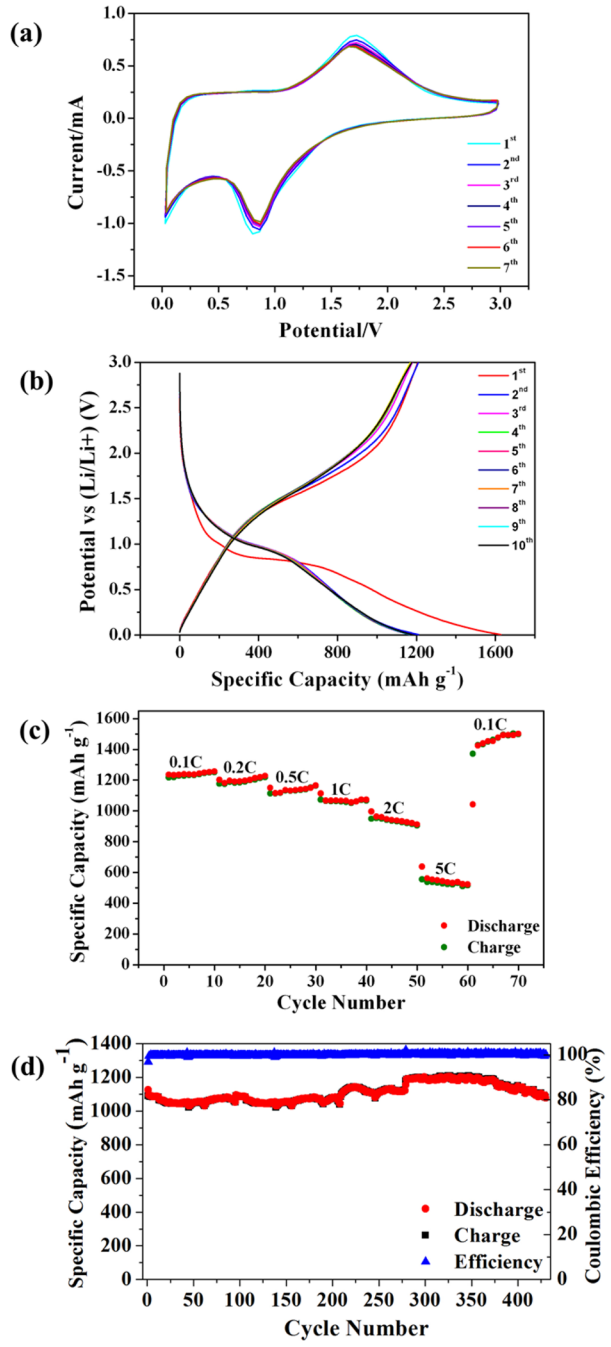

Figure 3. (a) Cyclic voltammetry profiles of $ZnFe_2O_4$/carbon nanocomposites for the first seven cycles between 0.005 and 3 V at a scan rate of 0.1 mV s^{-1}; (b) charge/discharge profiles of the $ZnFe_2O_4$/C nanocomposites electrode for the first 10 cycles between 0.005 and 3 V at specific current of 100 mA g^{-1}; (c) rate capability of $ZnFe_2O_4$(79.3 wt %)/carbon nanocomposites electrode tested under different current rates (1C = 1000 mA g^{-1}); (d) cycling performance of $ZnFe_2O_4$(79.3 wt %)/carbon nanocomposites tested at specific current of 200 mA g^{-1} (0.2C) for 430 cycles.

DOI: 10.1021/acsnano.5b07806
ACS Nano 2016, 10, 2728−2735

The rate performance of $ZnFe_2O_4$/carbon nanocomposites electrode was investigated by increasing the applied specific current every 10 cycles from 0.1C (1C = 1000 mA g^{-1}), 0.2C, 0.5C, 1C, and 2C to 5C and then back to 0.1C. The rate performances of the five $ZnFe_2O_4$/carbon nanocomposites electrodes with different $ZnFe_2O_4$ contents were compared (Figure S5). The best rate performance was achieved in $ZnFe_2O_4$(79.3 wt %)/carbon nanocomposites. Figure 3c depicts the rate performance for the $ZnFe_2O_4$(79.3 wt %)/carbon nanocomposites electrode. Clearly, the specific capacity decreased with the increase in specific current. Interestingly, the attractive capacities of 1238, 1198, 1136, 1052, 926, and 521 were achieved at specific currents of 100 (0.1C), 200 (0.2C), 500 (0.5C), 1000 (1C), 2000 (2C) and 5000 mA g^{-1} (5C), respectively. When the specific current returned to 0.1C, the capacities not only rebounded back to high value but also showed a continuous increase and reached a higher value of approximately 1500 mAh g^{-1} due to the gradual activation process.[1] Such outstanding rate performance can be ascribed to the synergistic effect of the presence of nanosized $ZnFe_2O_4$ particles and the continuous carbon network. The carbon network with good electrical conductivity served as the conductive medium between $ZnFe_2O_4$ nanoparticles and the current collectors; therefore, the fast charge−discharge can be realized.[32] In addition, the $ZnFe_2O_4$ nanoparticles with such a small size increased the interfacial area for Li reaction and shortened the transport length for ions and electrons, leading to high reversible capacities even at high specific currents.[48] The pure $ZnFe_2O_4$ nanoparticles (*i.e.*, in the absence of continuous carbon network) obtained by calcination in air were compared with the $ZnFe_2O_4$/C nanocomposites calcinated under argon. Figures 4a and 4b show the TEM image and the rate performance of pure $ZnFe_2O_4$ nanoparticles. Clearly, as compared with pure $ZnFe_2O_4$ nanoparticles, due to the presence of continuous and conductive carbon network in $ZnFe_2O_4$/carbon nanocomposites, their rate performance was markedly improved.

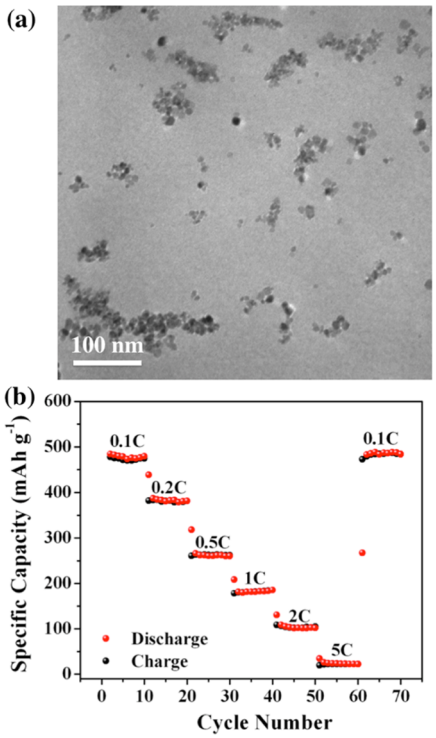

Figure 4. (a) TEM image of pure $ZnFe_2O_4$ nanoparticles obtained by calcinating the $ZnFe_2O_4$ precursors-loaded PS@PAA nanospheres in air. (b) Rate capability of pure $ZnFe_2O_4$ nanoparticles electrode tested under different current rates (1C = 1000 mA g^{-1}).

Figure 3d shows the galvanostatic cycling performance of the $ZnFe_2O_4$(79.3 wt %)/carbon nanocomposites electrode tested under specific current density of 200 mA g^{-1} over a voltage window between 0.005 and 3 V for 430 cycles. Prior to the leveling off, the discharge capacity gradually increased from initial value of 1090 mAh g^{-1} to around 1190 mAh g^{-1} for the first 280 cycles and reached a stable value of around 1190 mAh g^{-1} from 280 to 370 cycles. The rapid capacity decay was then observed after 370 cycles and the capacity decreased to about 1078 mAh g^{-1} after the cycling finished at 430 cycles, yielding a capacity retention of 98%. The observed capacity increase during cycling was commonly observed for graphene/carbon-based metal oxide composites and was attributed largely to the improved Li-diffusion kinetics due to the gradual activation process and reversible reaction between metal particles and electrolytes.[1] Such long-term cyclic stability demonstrated the excellent structural stability for the $ZnFe_2O_4$/carbon nanocomposites with $ZnFe_2O_4$ nanoparticles encapsulated in the carbon matrix.

The Nyquist electrochemical impedance spectra (EIS) of $ZnFe_2O_4$(79.3 wt %)/carbon nanocomposites electrode in the fresh state as well as after cycling (in the charged state) at 0.2C for 430 cycles are shown in Figure 5. The EIS spectra showed a

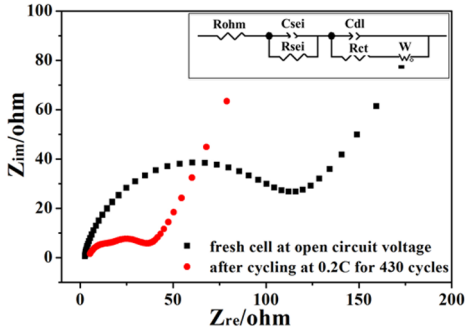

Figure 5. Electrochemical impedance spectra (Nyquist plot) of fresh and cycled $ZnFe_2O_4$(79.3 wt %)/carbon nanocomposites electrodes. The electrical equivalent circuit is shown as an inset.

quasi-semicircle from the high to intermediate frequency range and a straight slopping line in the low frequency range, similar to the previous detailed study.[54] The inset in Figure 5 illustrates the corresponding equivalent circuit model, where R_{ohm} is the ohmic resistance, reflecting a combined resistance of the electrolyte, separator, and electrodes. The semicircle in the high frequency range can be attributed to the resistance R_{sei} and the capacitance C_{sei} of the formation of the SEI layer. The semicircle in the intermediate frequency is associated with the charge-transfer resistance R_{ct} and its relative double-layer capacitance C_{dl}. The sloping line in the low frequency region is related to the Warburg impedance W, representing the lithium ion diffusion resistance in bulk electrode. From the EIS plots, it is clear that the radii of the quasi-semicircle after cycling is much smaller than that of fresh cell, which can be ascribed to the formation of SEI film and the activation process during cycling.[55]

DOI: 10.1021/acsnano.5b07806
ACS Nano 2016, 10, 2728−2735

After the cycling finished, the battery was dissembled inside the glovebox and the electrode was washed with dimethyl carbonate (DMC) rigorously for structural analysis. Figures 6a and 6b show the TEM images of the $ZnFe_2O_4$(79.3 wt %)/carbon nanocomposites after cycling. The structure of nanocomposites was seen to be retained after cycling with the continuous carbon network encapsulating the nanoparticles, except the nanoparticles turning into much smaller size after the repeated lithiation/delithiation. Such good structural stability rendered the prolonged cycling stability. Figure 6 panels c–f display the SEM images of the $ZnFe_2O_4$(79.3 wt %)/carbon nanocomposites electrode that was freshly prepared (Figure 6c,d) and after cycling (Figure 6e,f). No significant morphological change was observed after cycling, suggesting the good structural stability of the nanocomposites electrode. The SEM images (Figure 6e,f) for the electrode after cycling revealed that a uniform SEI layer resulting from the catalytically enhanced electrolyte reduction at low potential was formed on the $ZnFe_2O_4$/carbon nanocomposites surface. As a result, the morphology was changed from loose powder-like (Figure 6c,d) to self-holding appearance (Figure 6e,f),[56] thereby reducing the contact area between the active materials and the electrolyte by blocking some holes, which may be responsible for the capacity decay after 370 cycles.

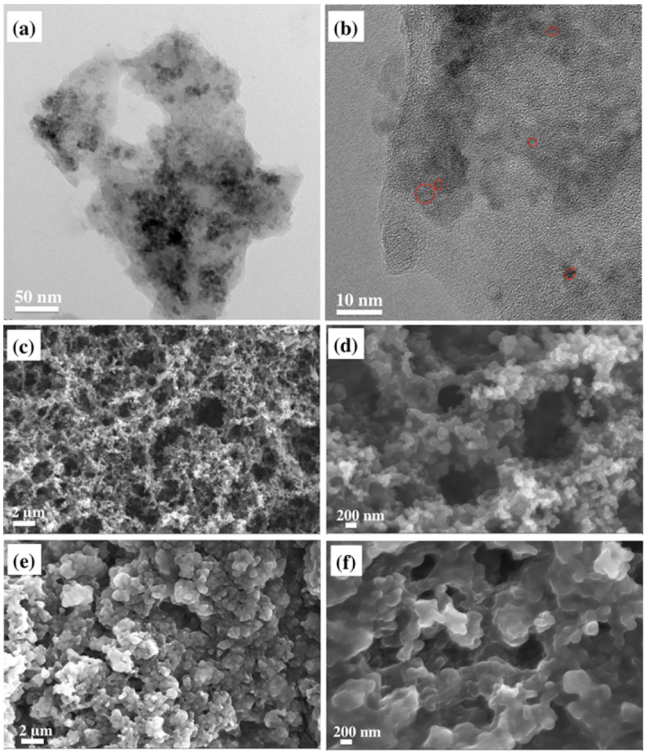

Figure 6. HRTEM images of $ZnFe_2O_4$(79.3 wt %)/carbon nanocomposites electrodes after cycling at 0.2C for over 400 cycles. (c,d) SEM images of freshly prepared $ZnFe_2O_4$(79.3 wt %)/carbon nanocomposites electrodes. (e,f) SEM images of $ZnFe_2O_4$(79.3 wt %)/carbon nanocomposites after cycling at 0.2C for over 400 cycles.

CONCLUSION

In summary, we developed a facile and effective strategy for *in situ* crafting $ZnFe_2O_4$/carbon nanocomposites electrode comprising 16 ± 5 nm $ZnFe_2O_4$ nanoparticles embedded within the continuous carbon network through the pyrolysis of $ZnFe_2O_4$ precursors-containing PS@PAA core@shell nanospheres. The advantages of this strategy are 3-fold. First, the PS@PAA nanosphere template is synthesized by emulsion polymerization in *one-step*. Second, the pyrolysis leads to the formation of $ZnFe_2O_4$ nanoparticles. Third, in the meantime the pyrolysis also induced the carbonization of PS@PAA, forming a continuous carbon network that encapsulates the formed $ZnFe_2O_4$ nanoparticles. Notably, the carbon network offers a continuous conductive pathway for electron transport, improves the mechanical flexibility of active materials, and more importantly, maintains the structural integrity of $ZnFe_2O_4$/carbon nanocomposites during repeated lithiation/delithiation. As anode materials for LIBs, the $ZnFe_2O_4$/C nanocomposites containing 79.3 wt % $ZnFe_2O_4$ exhibited the best electrochemical performance, delivering excellent rate performance with high capacities of 1238, 1198, 1136, 1052, 926, and 521 mAh g^{-1} at specific currents of 100, 200, 500, 1000, 2000, and 5000 mA g^{-}, respectively, and prolonged cycling stability over several hundred cycles. Such outstanding electrochemical performance of $ZnFe_2O_4$/carbon nanocomposites electrode is a direct consequence of the synergy of nanoscopic $ZnFe_2O_4$ particles and their hybridization with a continuous conductive carbon network. We envision that this simple and robust synthetic strategy can be readily extended for the preparation of other carbon hybridized electrode materials for high-performance LIBs.

EXPERIMENTAL SECTION

Synthesis of PS@PAA Nanospheres. PS@PAA nanospheres were prepared by emulsion polymerization of the mixture of styrene and acrylic acid in aqueous solution by modifying the method reported in the literature.[42] Typically, 2.176 g of acrylic acid was dissolved in 150 mL of DI water to form a homogeneous solution. A 10.4 g sample of styrene was then added to the above solution to form uniform oil-in-water droplets by stirring the mixture at 450 rpm for 30 min at room temperature, followed by the addition of 0.54 g of $K_2S_2O_8$. Subsequently, the mixture was degassed under an argon purge for 1 h. The polymerization was then performed by reacting at 80 °C for 24 h under vigorous magnetic stirring. For TEM imaging, a small portion of the resulting solution was diluted by water and casted onto the copper TEM grid for drying. The powder for FTIR characterization was obtained by centrifugation and then drying at 65 °C in vacuum oven.

Synthesis of $ZnFe_2O_4$ Precursors-Loaded PS@PAA Nanospheres. The precursors solution was prepared by dissolving $Zn(NO_3)_2{\cdot}6H_2O$ and $Fe(NO_3)_3{\cdot}9H_2O$ in DI water, and the pH for precursors solution was adjusted to be 2, consistent with the pH value of the PS@PAA solution. After the polymerization was complete by reacting for 24 h, the precursor solution was added dropwise into the solution under strong magnetic stirring and then stirred at 80 °C for 6 h to ensure the complete coordination between the carboxyl groups of PAA and the metal moieties of precursors. The solution was cooled down and diluted with DI water for TEM characterization. The precursors-loaded PS@PAA powder was obtained by centrifugation and then dried at 65 °C in a vacuum oven.

Synthesis of $ZnFe_2O_4$/Carbon Nanocomposites. The precursors-loaded PS@PAA powder was first ground by mortar and pestle. It was then heated at 1 °C/min to 600 °C for 2 h in a tubular furnace (MTI) under argon atmosphere. Finally, the obtained $ZnFe_2O_4$/carbon nanocomposites powder was ground for further characterization.

Characterizations. Transmission electron microscope (TEM) and HRTEM analysis were performed on samples deposited on a copper grid by JEOL TEM 100CX at an accelerating voltage of 100 kV. The cubic spinel structure of $ZnFe_2O_4$ was confirmed by powder X-ray diffraction (XRD) on an alpha-1 (Cu Kα, λ = 0.154 nm). The amorphous nature of the carbon network encapsulating the nano-

DOI: 10.1021/acsnano.5b07806
ACS Nano 2016, 10, 2728–2735

particles was confirmed by Raman spectroscopy using a Renishaw InVia Raman spectrometer equipped with a 785 nm laser. The morphology of the nanocomposites electrodes before and after cycling tests was analyzed by scanning electron microscopy (SEM; LEO 1530). FTIR studies were conducted over a wavenumber range of 400−4400 cm^{-1} (Shimadzu Japan) to evaluate the loading of $ZnFe_2O_4$ precursors within PS@PAA nanospheres. The weight ratio of the $ZnFe_2O_4$ nanoparticles was determined by thermogravimetric analysis (TGA) in air (TA Instruments Q5000).

Electrochemical Characterization. Electrochemical performance of electrodes was examined by galvanostatic testing of CR 2032-type coin cells assembled in an argon filled glovebox (MBraun). The coin cells used the $ZnFe_2O_4$/carbon nanocomposites as cathode, lithium foil as anode, and polypropylene (Celgard 2500, Celgard Inc., USA) as separator. The cathode was composed of 80 wt % of $ZnFe_2O_4$/C nanocomposites as active material, 10 wt % of acetylene black as conductive agent, and 10 wt % of polyvinylidene fluoride (PVDF) as binder. The electrolyte purchased was a 1 M $LiPF_6$ solution in the mixed solvents of ethylene carbonate (EC), diethyl carbonate (DEC), and ethyl methyl carbonate (EMC) (volume ratio = 1:1:1, 1 M $LiPF_6$/EC+DEC+EMC). The assembled cells were galvanostatically cycled between 0.005 and 3 V (Arbin battery testing system, BT2043) at room temperature. The cyclic voltammograms (CVs) were recorded using an IM6ex electrochemical workstation at a scan rate of 0.1 mV s^{-1} over the voltage window of 0.005 V−3.0 V. The electrochemical impedance spectroscopy (EIS) measurements were also performed on the IM6ex electrochemical workstation over a frequency range of 10^{-2}−10^5 Hz. A perturbation of 0.005 V was applied. After the cycling performance test, the fully charged coin cells were dissembled in the glovebox for further examination. The $ZnFe_2O_4$/carbon nanocomposites electrodes were rinsed using dimethyl carbonate (DMC) to remove the organic solvents and dissolved salts, and dried in the glovebox prior to examination.

ASSOCIATED CONTENT

Supporting Information

The Supporting Information is available free of charge on the ACS Publications website at DOI: 10.1021/acsnano.5b07806.

FTIR spectra of PS@PAA nanospheres before and after loading the $ZnFe_2O_4$ precursors, TGA plot of the $ZnFe_2O_4$ precursors-loaded PS@PAA nanospheres, EDX spectrum of the $ZnFe_2O_4$(79.3 wt %)/carbon nanocomposites, TGA plots of the $ZnFe_2O_4$/carbon nanocomposites, and rate capabilities of the five $ZnFe_2O_4$/carbon nanocomposites electrodes (PDF)

AUTHOR INFORMATION

Corresponding Author

*E-mail: zhiqun.lin@mse.gatech.edu.

Notes

The authors declare no competing financial interest.

REFERENCES

(1) Wu, R.; Wang, D. P.; Rui, X.; Liu, B.; Zhou, K.; Law, A. W. K.; Yan, Q.; Wei, J.; Chen, Z. *In-Situ* Formation of Hollow Hybrids Composed of Cobalt Sulfides Embedded within Porous Carbon Polyhedra/Carbon Nanotubes for High-Performance Lithium-Ion Batteries. *Adv. Mater.* **2015**, *27*, 3038−3044.

(2) Hou, L.; Lian, L.; Zhang, L.; Pang, G.; Yuan, C.; Zhang, X. Self-Sacrifice Template Fabrication of Hierarchical Mesoporous Bi-Component-Active Zno/$ZnFe_2O_4$ Sub-Microcubes as Superior Anode Towards High-Performance Lithium-Ion Battery. *Adv. Funct. Mater.* **2015**, *25*, 238−246.

(3) He, C.; Wu, S.; Zhao, N.; Shi, C.; Liu, E.; Li, J. Carbon-Encapsulated Fe_3O_4 Nanoparticles as a High-Rate Lithium Ion Battery Anode Material. *ACS Nano* **2013**, *7*, 4459−4469.

(4) Poizot, P.; Laruelle, S.; Grugeon, S.; Dupont, L.; Tarascon, J. M. Nano-Sized Transition-Metal Oxides as Negative-Electrode Materials for Lithium-Ion Batteries. *Nature* **2000**, *407*, 496−499.

(5) Bresser, D.; Paillard, E.; Kloepsch, R.; Krueger, S.; Fiedler, M.; Schmitz, R.; Baither, D.; Winter, M.; Passerini, S. Carbon Coated $ZnFe_2O_4$ Nanoparticles for Advanced Lithium-Ion Anodes. *Adv. Energy Mater.* **2013**, *3*, 513−523.

(6) Liu, J.; Zhang, H. G.; Wang, J.; Cho, J.; Pikul, J. H.; Epstein, E. S.; Huang, X.; Liu, J.; King, W. P.; Braun, P. V. Hydrothermal Fabrication of Three-Dimensional Secondary Battery Anodes. *Adv. Mater.* **2014**, *26*, 7096−7101.

(7) Han, C.; Yang, D.; Yang, Y.; Jiang, B.; He, Y.; Wang, M.; Song, A.-Y.; He, Y.-B.; Li, B.; Lin, Z. Hollow Titanium Dioxide Spheres as Anode Material for Lithium Ion Battery with Largely Improved Rate Stability and Cycle Performance by Suppressing the Formation of Solid Electrolyte Interface Layer. *J. Mater. Chem. A* **2015**, *3*, 13340−13349.

(8) Xiong, S.; Chen, J. S.; Lou, X. W.; Zeng, H. C. Mesoporous Co_3O_4 and CoO@C Topotactically Transformed from Chrysanthemum-Like $Co(Co_3)_{0.5}(Oh)\cdot 0.11H_2O$ and Their Lithium-Storage Properties. *Adv. Funct. Mater.* **2012**, *22*, 861−871.

(9) Zhou, G.; Wang, D. W.; Li, F.; Zhang, L.; Li, N.; Wu, Z. S.; Wen, L.; Lu, G. Q.; Cheng, H. M. Graphene-Wrapped Fe_3O_4 Anode Material with Improved Reversible Capacity and Cyclic Stability for Lithium Ion Batteries. *Chem. Mater.* **2010**, *22*, 5306−5313.

(10) Hu, Y. S.; Kienle, L.; Guo, Y. G.; Maier, J. High Lithium Electroactivity of Nanometer-Sized Rutile TiO_2. *Adv. Mater.* **2006**, *18*, 1421−1426.

(11) Jamnik, J.; Maier, J. Nanocrystallinity Effects in Lithium Battery Materials Aspects of Nano-Ionics. Part Iv. *Phys. Chem. Chem. Phys.* **2003**, *5*, 5215−5220.

(12) Yu, D.; Qiao, Y.; Zhou, X.; Wang, J.; Li, C.; Chen, C.; Huo, Q. Mica-Like Vanadium Pentoxide-Nanostructured Thin Film as High-Performance Cathode for Lithium-Ion Batteries. *J. Power Sources* **2014**, *266*, 1−6.

(13) Yao, X.; Kong, J.; Zhou, D.; Zhao, C.; Zhou, R.; Lu, X. Mesoporous Zinc Ferrite/Graphene Composites: Towards Ultra-Fast and Stable Anode for Lithium-Ion Batteries. *Carbon* **2014**, *79*, 493−499.

(14) Arico, A. S.; Bruce, P.; Scrosati, B.; Tarascon, J. M.; van Schalkwijk, W. Nanostructured Materials for Advanced Energy Conversion and Storage Devices. *Nat. Mater.* **2005**, *4*, 366−377.

(15) Jiang, C.; Ichihara, M.; Honma, I.; Zhou, H. Effect of Particle Dispersion on High Rate Performance of Nano-Sized $Li_4Ti_5O_{12}$ Anode. *Electrochim. Acta* **2007**, *52*, 6470−6475.

(16) Larcher, D.; Masquelier, C.; Bonnin, D.; Chabre, Y.; Masson, V.; Leriche, J.-B.; Tarascon, J.-M. Effect of Particle Size on Lithium Intercalation into α-Fe_2O_3. *J. Electrochem. Soc.* **2003**, *150*, A133−A139.

(17) Morales, J.; Sánchez, L.; Martín, F.; Berry, F.; Ren, X. Synthesis and Characterization of Nanometric Iron and Iron-Titanium Oxides by Mechanical Milling:: Electrochemical Properties as Anodic Materials in Lithium Cells. *J. Electrochem. Soc.* **2005**, *152*, A1748−A1754.

(18) Chen, J.; Xu, L.; Li, W.; Gou, X. A-Fe2o3 Nanotubes in Gas Sensor and Lithium-Ion Battery Applications. *Adv. Mater.* **2005**, *17*, 582−586.

(19) Shaju, K. M.; Jiao, F.; Debart, A.; Bruce, P. G. Mesoporous and Nanowire Co_3O_4 as Negative Electrodes for Rechargeable Lithium Batteries. *Phys. Chem. Chem. Phys.* **2007**, *9*, 1837−1842.

(20) Li, Y.; Tan, B.; Wu, Y. Mesoporous Co_3O_4 Nanowire Arrays for Lithium Ion Batteries with High Capacity and Rate Capability. *Nano Lett.* **2008**, *8*, 265−270.

(21) Li, W. Y.; Xu, L. N.; Chen, J. Co_3O_4 Nanomaterials in Lithium-Ion Batteries and Gas Sensors. *Adv. Funct. Mater.* **2005**, *15*, 851−857.

(22) Zhang, W. M.; Wu, X. L.; Hu, J. S.; Guo, Y. G.; Wan, L.-J. Carbon Coated Fe_3O_4 Nanospindles as a Superior Anode Material for Lithium-Ion Batteries. *Adv. Funct. Mater.* **2008**, *18*, 3941−3946.

DOI: 10.1021/acsnano.5b07806
ACS Nano 2016, 10, 2728−2735

(23) Zhan, F.; Geng, B.; Guo, Y. Porous Co_3O_4 Nanosheets with Extraordinarily High Discharge Capacity for Lithium Batteries. *Chem. - Eur. J.* **2009**, *15*, 6169−6174.
(24) Tang, K.; Fu, L.; White, R. J.; Yu, L.; Titirici, M.-M.; Antonietti, M.; Maier, J. Hollow Carbon Nanospheres with Superior Rate Capability for Sodium-Based Batteries. *Adv. Energy Mater.* **2012**, *2*, 873−877.
(25) Wu, S.; Xu, R.; Lu, M.; Ge, R.; Iocozzia, J.; Han, C.; Jiang, B.; Lin, Z. Graphene-Containing Nanomaterials for Lithium-Ion Batteries. *Adv. Energy Mater.* **2015**, *5*, 1500400.
(26) Ji, L.; Lin, Z.; Alcoutlabi, M.; Zhang, X. Recent Developments in Nanostructured Anode Materials for Rechargeable Lithium-Ion Batteries. *Energy Environ. Sci.* **2011**, *4*, 2682−2699.
(27) Wang, Y.; Wang, Y.; Hosono, E.; Wang, K.; Zhou, H. The Design of a $LiFePO_4$/Carbon Nanocomposite with a Core−Shell Structure and Its Synthesis by an *in Situ* Polymerization Restriction Method. *Angew. Chem., Int. Ed.* **2008**, *47*, 7461−7465.
(28) Liu, X.-m.; Yan, P.; Xie, Y.-Y.; Yang, H.; Shen, X.-d.; Ma, Z.-F. Synthesis of Superior Fast Charging-Discharging Nano-$LiFePO_4$/C from Nano-$FePO_4$ Generated Using a Confined Area Impinging Jet Reactor Approach. *Chem. Commun.* **2013**, *49*, 5396−5398.
(29) Cheng, L.; Yan, J.; Zhu, G. N.; Luo, J. Y.; Wang, C. X.; Xia, Y. Y. General Synthesis of Carbon-Coated Nanostructure $Li_4Ti_5O_{12}$ as a High Rate Electrode Material for Li-Ion Intercalation. *J. Mater. Chem.* **2010**, *20*, 595−602.
(30) Yao, L.; Hou, X.; Hu, S.; Tang, X.; Liu, X.; Ru, Q. An Excellent Performance Anode of $ZnFe_2O_4$/Flake Graphite Composite for Lithium Ion Battery. *J. Alloys Compd.* **2014**, *585*, 398−403.
(31) Xia, H.; Qian, Y.; Fu, Y.; Wang, X. Graphene Anchored with $ZnFe_2O_4$ Nanoparticles as a High-Capacity Anode Material for Lithium-Ion Batteries. *Solid State Sci.* **2013**, *17*, 67−71.
(32) Kong, J.; Yao, X.; Wei, Y.; Zhao, C.; Ang, J. M.; Lu, X. Polydopamine-Derived Porous Nanofibers as Host of Znfe2o4 Nanoneedles: Towards High-Performance Anodes for Lithium-Ion Batteries. *RSC Adv.* **2015**, *5*, 13315−13323.
(33) Wang, H.; Cui, L. F.; Yang, Y.; Sanchez Casalongue, H.; Robinson, J. T.; Liang, Y.; Cui, Y.; Dai, H. Mn_3O_4−Graphene Hybrid as a High-Capacity Anode Material for Lithium Ion Batteries. *J. Am. Chem. Soc.* **2010**, *132*, 13978−13980.
(34) Zhou, J.; Song, H.; Chen, X.; Zhi, L.; Yang, S.; Huo, J.; Yang, W. Carbon-Encapsulated Metal Oxide Hollow Nanoparticles and Metal Oxide Hollow Nanoparticles: A General Synthesis Strategy and Its Application to Lithium-Ion Batteries. *Chem. Mater.* **2009**, *21*, 2935−2940.
(35) Paek, S. M.; Yoo, E.; Honma, I. Enhanced Cyclic Performance and Lithium Storage Capacity of SnO_2/Graphene Nanoporous Electrodes with Three-Dimensionally Delaminated Flexible Structure. *Nano Lett.* **2009**, *9*, 72−75.
(36) Luo, Y.; Luo, J.; Zhou, W.; Qi, X.; Zhang, H.; Yu, D. Y. W.; Li, C. M.; Fan, H. J.; Yu, T. Controlled Synthesis of Hierarchical Graphene-Wrapped TiO_2@Co_3O_4 Coaxial Nanobelt Arrays for High-Performance Lithium Storage. *J. Mater. Chem. A* **2013**, *1*, 273−281.
(37) Heidari, E. K.; Zhang, B.; Sohi, M. H.; Ataie, A.; Kim, J. K. Sandwich-Structured Graphene-$NiFe_2O_4$-Carbon Nanocomposite Anodes with Exceptional Electrochemical Performance for Li Ion Batteries. *J. Mater. Chem. A* **2014**, *2*, 8314−8322.
(38) Chang, J.; Huang, X.; Zhou, G.; Cui, S.; Hallac, P. B.; Jiang, J.; Hurley, P. T.; Chen, J. Multilayered Si Nanoparticle/Reduced Graphene Oxide Hybrid as a High-Performance Lithium-Ion Battery Anode. *Adv. Mater.* **2014**, *26*, 758−764.
(39) Pang, X.; Zhao, L.; Han, W.; Xin, X.; Lin, Z. A General and Robust Strategy for the Synthesis of Nearly Monodisperse Colloidal Nanocrystals. *Nat. Nanotechnol.* **2013**, *8*, 426−431.
(40) Jiang, B.; Pang, X.; Li, B.; Lin, Z. Organic−Inorganic Nanocomposites *via* Placing Monodisperse Ferroelectric Nanocrystals in Direct and Permanent Contact with Ferroelectric Polymers. *J. Am. Chem. Soc.* **2015**, *137*, 11760−11767.
(41) Chern, C. S. Emulsion Polymerization Mechanisms and Kinetics. *Prog. Polym. Sci.* **2006**, *31*, 443−486.
(42) Wen, F.; Zhang, W.; Zheng, P.; Zhang, X.; Yang, X.; Wang, Y.; Jiang, X.; Wei, G.; Shi, L. One-Stage Synthesis of Narrowly Dispersed Polymeric Core-Shell Microspheres. *J. Polym. Sci., Part A: Polym. Chem.* **2008**, *46*, 1192−1202.
(43) Xu, H.; Xu, Y.; Pang, X.; He, Y.; Jung, J.; Xia, H.; Lin, Z. A General Route to Nanocrystal Kebabs Periodically Assembled on Stretched Flexible Polymer Shish. *Sci. Adv.* **2015**, *1*, e1500025.
(44) Chen, C.; Li, R.; Xu, L.; Yan, D. Three-Dimensional Superhydrophobic Porous Hybrid Monoliths for Effective Removal of Oil Droplets from the Surface of Water. *RSC Adv.* **2014**, *4*, 17393−17400.
(45) Zhang, W.; Zhang, A.; Guan, Y.; Zhang, Y.; Zhu, X. X. Silver-Loading in Uncrosslinked Hydrogen-Bonded Lbl Films: Structure Change and Improved Stability. *J. Mater. Chem.* **2011**, *21*, 548−555.
(46) Huang, H.; Ji, Y.; Qiao, Z.; Zhao, C.; He, J.; Zhang, H. Preparation, Characterization, and Application of Magnetic Fe-Sba-15 Mesoporous Silica Molecular Sieves. *J. Autom. Methods Manage. Chem.* **2010**, *2010*, 323509.
(47) Illán-Gómez, M. J.; Raymundo-Piñero, E.; García-García, A.; Linares-Solano, A.; Salinas-Martínez de Lecea, C. Catalytic Nox Reduction by Carbon Supporting Metals. *Appl. Catal., B* **1999**, *20*, 267−275.
(48) Yao, L.; Hou, X.; Hu, S.; Wang, J.; Li, M.; Su, C.; Tade, M. O.; Shao, Z.; Liu, X. Green Synthesis of Mesoporous $ZnFe_2O_4$/C Composite Microspheres as Superior Anode Materials for Lithium-Ion Batteries. *J. Power Sources* **2014**, *258*, 305−313.
(49) Xu, J.; Jeon, I. Y.; Seo, J. M.; Dou, S.; Dai, L.; Baek, J.-B. Edge-Selectively Halogenated Graphene Nanoplatelets (Xgnps, X = Cl, Br, or I) Prepared by Ball-Milling and Used as Anode Materials for Lithium-Ion Batteries. *Adv. Mater.* **2014**, *26*, 7317−7323.
(50) Hu, X.; Lin, Z.; Yang, K.; Huai, Y.; Deng, Z. Effects of Carbon Source and Carbon Content on Electrochemical Performances of $Li_4Ti_5O_{12}$/C Prepared by One-Step Solid-State Reaction. *Electrochim. Acta* **2011**, *56*, 5046−5053.
(51) Cho, Y. D.; Fey, G. T.K.; Kao, H. M. The Effect of Carbon Coating Thickness on the Capacity of $LiFePO_4$/C Composite Cathodes. *J. Power Sources* **2009**, *189*, 256−262.
(52) Deng, Y.; Zhang, Q.; Tang, S.; Zhang, L.; Deng, S.; Shi, Z.; Chen, G. One-Pot Synthesis of $ZnFe_2O_4$/C Hollow Spheres as Superior Anode Materials for Lithium Ion Batteries. *Chem. Commun.* **2011**, *47*, 6828−6830.
(53) Ding, Y.; Yang, Y.; Shao, H. High Capacity $ZnFe_2O_4$ Anode Material for Lithium Ion Batteries. *Electrochim. Acta* **2011**, *56*, 9433−9438.
(54) Martinez-Julian, F.; Guerrero, A.; Haro, M.; Bisquert, J.; Bresser, D.; Paillard, E.; Passerini, S.; Garcia-Belmonte, G. Probing Lithiation Kinetics of Carbon-Coated $ZnFe_2O_4$ Nanoparticle Battery Anodes. *J. Phys. Chem. C* **2014**, *118*, 6069−6076.
(55) Hou, X.; Hu, Y.; Jiang, H.; Li, Y.; Li, W.; Li, C. One-Step Synthesis of Snox Nanocrystalline Aggregates Encapsulated by Amorphous TiO_2 as an Anode in Li-Ion Battery. *J. Mater. Chem. A* **2015**, *3*, 9982−9988.
(56) Wu, H.; Chan, G.; Choi, J. W.; Ryu, I.; Yao, Y.; McDowell, M. T.; Lee, S. W.; Jackson, A.; Yang, Y.; Hu, L.; Cui, Y. Stable Cycling of Double-Walled Silicon Nanotube Battery Anodes through Solid-Electrolyte Interphase Control. *Nat. Nanotechnol.* **2012**, *7*, 310−315.

DOI: 10.1021/acsnano.5b07806
ACS Nano 2016, 10, 2728−2735